Experimental and Computational Investigation of Flow Instabilities in Turbine Rim Seals

Joshua TM Horwood, Fabian P Hualca, James A Scobie, Michael Wilson, Carl M Sangan and Gary D Lock
j.t.m.horwood@bath.ac.uk, f.hualca@bath.ac.uk, j.a.scobie@bath.ac.uk, m.wilson@bath.ac.uk, c.m.sangan@bath.ac.uk and g.d.lock@bath.ac.uk
Department of Mechanical Engineering
University of Bath
Bath, BA2 7AY
United Kingdom

ABSTRACT

In high-pressure turbines, cool air is purged through rim seals at the periphery of wheel-spaces between the stator and rotor discs. The purge suppresses the ingress of hot gas from the annulus but superfluous use is inefficient. In this paper the interaction between the ingress, purge and mainstream flow is studied through comparisons of newly acquired experimental results alongside unsteady numerical simulations based on the DLR TRACE solver. New experimental measurements were taken from a one-and-a-half stage axial-turbine rig operating with engine-representative blade and vane geometries, and overlapping rim seals. Radial traverses using a miniature CO_2 concentration probe quantified the penetration of ingress into the rim seal and the outer portion of the wheel-space. Unsteady pressure measurements from circumferentially-positioned transducers on the stator disc identified distinct frequencies in the wheel-space, and the computations reveal these are associated with large-scale flow structures near the outer periphery rotating at just less than the disc speed. It is hypothesised that the physical origin of such phenomenon is driven by Kelvin-Helmholtz instabilities caused by the tangential shear between the annulus and egress flows, as also postulated by previous authors. The presence and intensity of these rotating structures are strongly dependent on the purge flow rate. While there is general qualitative agreement between experiment and computation, it is speculated that the under-prediction by the

computations of the measured levels of ingress is caused by deficiencies in the turbulence modelling.

1 INTRODUCTION

The latest generation of industrial gas turbines can offer combined-cycle efficiencies > 60% [1]. The secondary-air system has a fundamental role in determining this efficiency as well as component lifetime and integrity. Designers divert relatively cool purge from the compressor to pressurise the wheel-space between the stator and rotor discs, reducing the ingress of hot gases through rim seals. This purge, or sealing flow, should be minimised as it draws air away from power generation as well as generating aerodynamic mixing losses in the annulus.

Ingress through clearance seals is governed by the complex, unsteady, three-dimensional flow field created by the vanes and rotating blades. Reliably modelling such flows using computational fluid dynamics (CFD) has been difficult, even with Large-Eddy Simulations (LES) and 360º Unsteady Reynolds-Averaged Navier-Stokes (URANS) calculations; these models currently require significant computational resources which, arguably, limit their value as a tool for the engine designer. A further challenge lies in the simultaneous computation of short timescales in the annulus flow alongside the longer timescales associated with the convection of ingress around the wheel-space.

One common finding in recent research (both computational and experimental) is that the rim-seal and wheel-space flows are observed to contain a range of frequencies below the blade passing frequency. These have been shown to correspond to structures that vary in number (N, a fraction of the blade count) and speed (ω), and which are important to the fluid mechanics of ingress. This paper explores the influence of these

rotating structures using newly acquired experimental data, and compares the results to a complementary reduced computational domain (22.5^o versus 360^o).

Section 2 is a review of the relevant literature. A description of the computational model, experimental test facility and operating conditions is given in Section 3. Section 4 discusses time-averaged results of pressure, swirl and sealing effectiveness. Section 5 discusses the unsteady flow phenomena, including an analysis of numerical and experimental pressure data. The principal conclusions are given in Section 6.

2 LITERATURE REVIEW

This review focusses mainly on CFD studies of ingress. An extensive review of one-dimensional models along with experimental work was provided by Scobie et al. [2]. Two non-dimensional flow rates (Φ_0 and λ_T) defined in the nomenclature govern, respectively, these inviscid and viscous phenomena.

Early computational studies of ingress used steady methods [e.g., 3]. However, Hills et al. [4] along with Laskowski et al. [5] both determined that unsteady CFD was required to adequately capture the unstable flows close to the rim seal and that these had a significant effect on driving ingress.

In addition to the interaction between vanes and blades, recent computational and experimental work has identified large-scale unsteady flow structures occurring at frequencies unrelated to those of the blades.

Figure 1 illustrates data from the literature showing the number of structures identified (N), against their rotational speed relative to the disc (ω/Ω). The majority of studies, including all experimental data, have found 8-30 structures rotating at 75-100% of the disc speed, over a wide range of different geometries and flow conditions. The computational and experimental results from this paper have been added. The breadth

of data suggests the structures are physical and not simply an anomaly of one particular experimental facility or computational circumstance. There is a weak negative correlation between the two variables (N and ω/Ω), though further investigation would be required to confirm this.

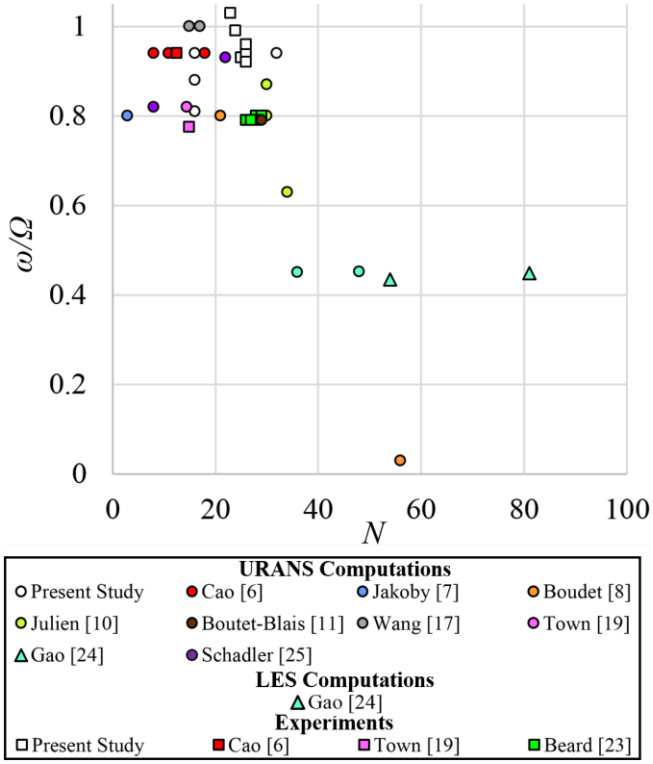

Figure 1: Comparison of rotating low-pressure structures from literature

To the author's knowledge, Cao et al. [6] was the first to demonstrate the existence of the unsteady flow features categorised in Figure 1. Their computations captured low-pressure structures within an axial clearance rim seal, despite removing vanes and blades from the model. These numerical simulations were validated using fast-response pressure transducers, with both experiments and CFD showing $8 < N < 18$ structures rotating at 90-94% of the disc speed. The authors also showed the characteristics of the rotating structures (N and ω/Ω) were a function of geometry and their intensity was supressed with a reduction in the axial clearance of the seal or an increase in the purge level. Jakoby et al. [7] also conducted ingress computations without blades or vanes;

using a 360º model, three large, low-pressure regions rotating at 80% of the disk speed were identified, but these structures were suppressed at higher purge flow rates. These structures propagate deep into the cavity, indicating a potential cavity mode. It should be noted that this is distinct from the other instabilities discussed in this review, whilst potentially excited by the same phenomena.

Boudet et al. [8, 9] investigated ingress using unsteady CFD configurations with and without blades. Using a small 13.33º sector they computed rim-seal instabilities at 0.44 of the blade passing frequency (BPF), showing these rotating structures disappeared at higher sealing flow rates. They related their findings to Taylor-Couette instabilities and argued that they were supressed at higher purge rates due to a dominant centrifugal flow.

Julien et al. [10] and Boutet-Blais et al. [11] produced numerical simulations based on earlier experimental work by Feiereisen et al. [12]. Using a 74º sector model with nine vanes and 12 blades, Julien et al. identified 30-34 large-scale structures rotating at an angular speed slightly less than the disc speed. These structures were strongest at the no-purge and low-purge conditions tested and led to deep ingestion into the wheel-space; in contrast the vane-blade interaction which dominated at high purge led to only a shallow penetration of ingress into the upper region of the cavity. Boutet-Blais et al. used a 180º sector without vanes or blades alongside a 24º sector with blades and vanes. The larger model identified $24 < N < 28$ structures rotating around the entire disc, while the smaller sector computed 29. Importantly, the work also showed that a passive scalar-based ingress model compared very well against a temperature-based version, and concluded that using a passive scalar in a cold rig was an adequate means to compare rim-seal designs.

Rabs et al. [13] studied the existence of Kelvin-Helmholtz instabilities in rim-seal flows. They showed that coherent vortex structures were generated due to an unstable shear layer between the purge and tangential annulus flow. Although the presence of vanes and blades supressed these instabilities, they did occur at the highest purge rate tested.

Chilla et al. [14] also discussed the formation of Kelvin- Helmholtz instabilities in the rim seal of a realistic turbine configuration. These instabilities were governed by the velocity deficit of the sealing flow relative to the mainstream and could be stabilised by increasing the sealing tangential velocity or the sealant mass flow. The work also showed that the rim-seal unsteadiness is shed into the rotor hub endwall at a frequency below the vane passing frequency, and could lead to increased loss within the turbine stage.

Large Eddy Simulations (LES) of ingress were performed by O'Mahoney et al. [15, 16] using the same geometry as earlier studies by Boudet et al. [8, 9]. The work found that increasing the sector size from 13.3º to 40º had little effect on the average flow fields, while LES showed an improved prediction of ingress relative to URANS. It should be noted that even the smallest LES computation required 20 days on 256 processors, while the corresponding URANS computation took just 14 days on 32 processors.

A comparison of full 360º URANS computations of ingress alongside an individual blade/vane passage model was conducted by Wang et al. [17]. Unlike O'Mahoney et al. their 360º model produced significantly-improved agreement with experiments; with much higher levels of ingestion, potentially driven by the 15-17 rotating pressure structures found circumferentially distributed around the seal region. The structures moved at approximately the disc speed and the authors concluded they could not have

developed in a small-sector model. Mirzamoghadam et al. [18] were later critical, stating that the six revolutions computed were insufficient for the structures to stabilize. Mirzamoghadam et al. also used 360º URANS numerical simulation of the same rig (albeit with a different seal geometry) and computed 6-8 structures, which were still evolving after sixteen disc revolutions.

Subsequent work by other authors continued the use of sector models and also identified large rotating structures. Using a 99.31º sector with eight vanes and ten blades, Town et al. [19] identified 14.5 structures moving at 81.7% of the disc speed; this compared well to the 15 structures rotating at 77.5% of the disc speed measured in their corresponding experiments. However, the work makes no mention of sealing effectiveness and results are only presented at one operating condition. The authors themselves also state that the experimental data would benefit from increased scrutiny.

A purely experimental study by Savov et al. [20] tested two different seal configurations, with and without blades over a range of conditions. The work identified a band of frequencies in the rim seal at $f / f_d \sim$ 20-40, that were attributed to an unstable shear layer as also identified by Rabs et al. For a single lip rim-seal, the unsteadiness was found to be suppressed by the presence of the blades, again reflecting the previous findings of Rabs et al. Savov et al. measured lower sealing effectiveness and intensified spectral activity at lower disc speeds (where the shear between annulus and wheel-space flows would be higher) and decreasing unsteadiness with decreasing ingestion at higher disc speeds, thus giving an indication of the importance of these unsteady structures.

Savov and Atkins [21] discuss a gap recirculation zone (GRZ) in the seal clearance, which is modulated by structures of differing length scales and the size of which is influenced by the purge flow rate. The authors developed a low order model that

considers not only the vane and blade scales but also those associated with shear-layer roll-up (i.e. Kelvin-Helmholtz instabilities) and large-scale non-uniformities.

Zlatinov et al. [22] used a computational model alongside an analytical model to demonstrate that in the presence of a rotating external pressure non-uniformity (such as that caused by rotor blades) pre-swirled purge flow can lead to increased levels of ingestion. It is reasoned that swirled purge flow more closely follows the rotor pressure field and responds more readily than non-swirled flow which is influenced by an average of multiple blade passes. The model is also extended to a case where ingestion is dominated by an unsteady pressure non-uniformity introduced by stator vanes and finds that under these conditions pre-swirl can reduce ingestion levels.

Beard et al. [23] conducted an experimental study on a one-stage turbine rig without blades or vanes, investigating solely the unsteady pressure field in the rim seal and cavity. The strongest unsteadiness was measured towards the outer periphery of the rim seal where a broad spectrum of activity was identified. The number of low-pressure structures within the rim-seal were shown to reduce from N = 28/29 to 26/27 as the purge level was reduced from its maximum level down to zero. The structures were measured to rotate at 80% of the disc speed and this was insensitive across the conditions tested. Gao et al. [24] later performed an LES and URANS study of the experiments conducted by Beard et al. The LES study used a 13.33º sector and captured approximately the same peak frequency at 23.5 times the disc speed; however, while the experiments showed this corresponded to 29 low-pressure structures rotating at 80% of the disc speed, the computations determined 54 structures rotating at 43.5% of the disc speed. It was suggested this discrepancy may have been caused by the small sector angle used in the LES. Despite using a larger sector size of 30º, a URANS simulation showed no better agreement with the experiments.

A combined experimental and computational study focussing on the influence of the unsteady rim-seal/cavity flow on the annulus flow was presented by Schadler et al. [25]. The CFD model identified 8-22 pressure structures rotating at 82-93% of the disc speed and like previous studies [e.g., 7, 8, 10, 14] this low-frequency unsteadiness was found to disappear at the highest purge rates. Schadler et al. also identified that the rim-seal unsteadiness could give rise to non-negligible noise-emission within the human perception of sound.

3 TEST RIG AND NUMERICAL MODEL

The computations undertaken for this study were based on the geometry and flow conditions found in the University of Bath turbine test facility. A brief overview of the experimental facility is given here; full details of the rig design and capabilities have been presented by Patinios et al. [26] and Scobie et al. [27].

3.1 Experimental Facility

The test facility experimentally models ingress into the upstream and downstream wheel-spaces of a one-and-a-half-stage axial turbine. The rig was specifically designed for instrumentation access in a fluid-dynamically-scaled environment of incompressible flow at low rotational Reynolds number; the design offers an efficient, expedient and inexpensive means of assessing new rim seal design concepts.

The test section is shown in Figure 2 and contains 32 upstream vanes, 48 turned rotor blades and 32 downstream vanes. The turbine geometry was designed by Siemens, replicating an operating engine. The diameter of the disc to the underside of the rim seal shroud is 380 mm and the height of the annulus is 25 mm. The rotor blisc (bladed disc) can be rotated up to 4000 rpm, providing a rotational Reynolds number, $Re_\phi = 1$

$\times 10^6$. Detachable aluminium seals on both the stationary and rotating sides of each wheel-space allow for flexible operation and access. This study used the generic double-overlap seal shown in Figure 4.

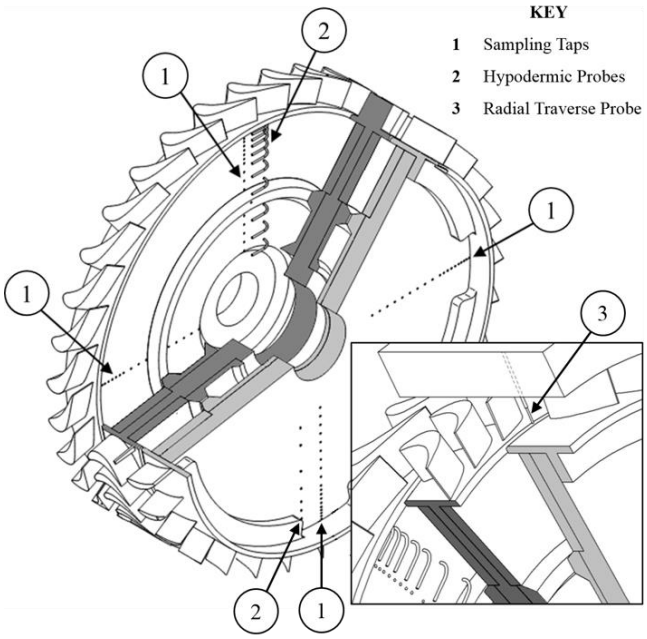

Figure 2: The Bath 1.5 stage turbine facility: test section and instrumentation

Purge is introduced to the rig at low radius, seeded with 1% CO_2 for measurements of concentration-based sealing effectiveness. Taps on the stator disc (labelled 1 in Fig. 2) and hypodermic-tubes as sampling inlets (labelled 2) were used to determine the radial variation of effectiveness and rotating core. Concentration was also collected along a radial traverse of the mainstream annulus and into the rim-seal region. The probe was a simple, miniature, stainless-steel hypodermic tube of 1.0 mm outer diameter. The traverse from the outer casing of the annulus to the seal clearance is illustrated as an inset (and labelled 3) in Figure 2. A larger hypodermic tube (1.7 mm diameter) was used by Scobie et al. to demonstrate the probe and gas-extraction rate did not influence the data collected.

Two Kulite XCS-062 pressure transducers were installed into the stator to measure unsteady pressure in the wheel-space. These transducers were circumferentially-located 8º apart at a radial height of r/b = 0.993, and sampled data at 100 kHz. At 4000 rpm the BPF is 3.2 kHz, which is significantly lower than the manufacturer-quoted resonant frequency of 150 kHz. Time-averaged static pressure can also be measured using the taps in the stator disc and circumferentially across a vane pitch on the annulus hub. Swirl was determined using total pressure from pitot tubes in the wheel-space core.

Owen and Rogers [28] have shown the flow structure in the wheel-space is governed by the turbulent flow parameter, λ_T. Although the experimental facility cannot match the high Reynolds numbers experienced in engines ($Re_\phi > 107$), the range of λ_T tested was chosen to match engine representative values. The two mainstream-flow conditions used for the experiments are shown in Table 1; these are at a common stage-design flow coefficient, but at two different rotational speeds and corresponding Re_ϕ. Computations were only conducted at the higher Reynolds number and for the upstream wheel-space.

Parameter	**Disk Speed (RPM)**	
	3000	**4000**
Rotational Reynolds number, Re_ϕ	7.2×10^5	1.0×10^6
Axial Reynolds number, Re_w	2.8×10^5	4.0×10^5
Flow coefficient, C_F	0.40	
Vane exit Mach number, M	0.33	0.44
Turbulent flow parameter, λ_T	$0 \rightarrow 0.22$	
Non-dimensional sealing parameter, Φ_0	$0 \rightarrow 0.21$	

Table 1: Operating conditions

3.2 Computational Model

Computations were undertaken using Turbomachinery Research Aerodynamics Computational Environment (TRACE) v9.0, a CFD package developed at the German Aerospace Center's (DLR) Institute of Propulsion Technology in Cologne, Germany. The compressible Reynolds-Averaged Navier-Stokes (RANS) solver uses a finite-

volume approach, with the second-order Fromm and Euler backward schemes chosen for spatial and temporal discretization respectively. The computations are all unsteady but required steady-state, mixing-plane solutions for initialisation.

The SST turbulence model was employed with the Kato-Launder modification to limit the production of turbulent kinetic energy. An additional transport equation for a passive scalar (analogous to the CO_2 in the experiments) was used to calculate the concentration-based sealing effectiveness. A sensitivity study identified that a minimum of 80 time-steps per blade pass were required for the unsteady solution to be invariant to an increasing number time-steps. In addition, the dual time-stepping scheme used 20 sub-iterations and a Courant Friedrich Levy number of 100.

Structured grid generation was undertaken using NUMECA AutoGrid5. The computational domain incorporated two upstream vanes, three blades and a wheel-space in a 22.5º sector as shown in Figure 3. A larger, 66.5º sector with six vanes and nine blades was also modelled at one sealing flow rate to investigate the influence of sector size. A 'zonal' non-matching grid interface was defined between the stationary and rotating domains, allowing unsteady coupling of field variables in two dimensions. This stator-rotor interface was placed 1 mm (= s_c /2) upstream of the seal. This avoided locating the interface in the highly unstable region immediately downstream of the seal and left the wheel-space in the rotating domain. A non-matching grid interface was used in the tip-clearance to improve cell quality through the rotor passage. Sealant flow enters at low radius through an extended narrow section to encourage Couette flow to develop properly before entering the main wheel-space. Mass flow, total temperature, turbulence intensity, turbulent-length scale and flow angles were specified at the inlet. The same parameters were defined at the stage inlet, with total pressure specified rather than mass flow. Static pressure was specified at stage exit. The standard 22.5º mesh has

a total cell count of 5.2 million, with 60 cells spaced circumferentially across each blade passage and 15 across the tip-clearance. Detail of the mesh is shown in Figure 4. A y+ ≈ 1 was used within the wheel-space and on the annulus hub, while a larger value of y+ ≈ 25, requiring wall functions, was employed on the blade and shroud walls. A grid-sensitivity study was undertaken to validate the suitability of the mesh resolution. Additional coarse and fine grids were generated using a refinement factor of 1.5 (in each direction) between each grid level. The grids were solved using a steady mixing plane solution. Profiles of pressure and velocity throughout the domain were compared across grids, with significant discrepancies existing between the coarse and baseline grid levels but no distinguishable differences between the baseline and fine grids.

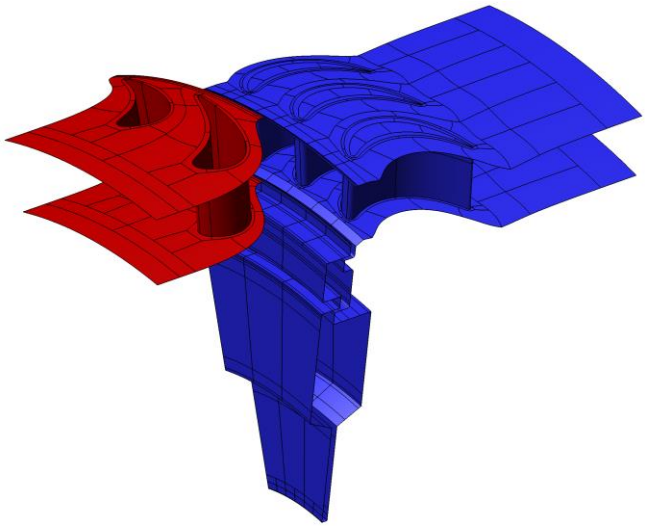

Figure 3: Computational domain

All computations produced average residual levels < 10^{-6} and maximum residual levels < 10^{-3}. Convergence was defined by a change of < 1% in the passive scalar over 20,000 time-steps, along with periodic, unchanging behaviour of all other variables. The relatively slow convergence of the passive scalar is a consequence of the large difference in time-scales between annulus and cavity flows, which causes slow convection of the scalar around the wheel-space. The computations using the lowest

sealing flow rate demanded the largest computational effort, with the most expensive computations requiring ≈ 20,000 core hours, corresponding to ≈ 13.2 revolutions of the rotor.

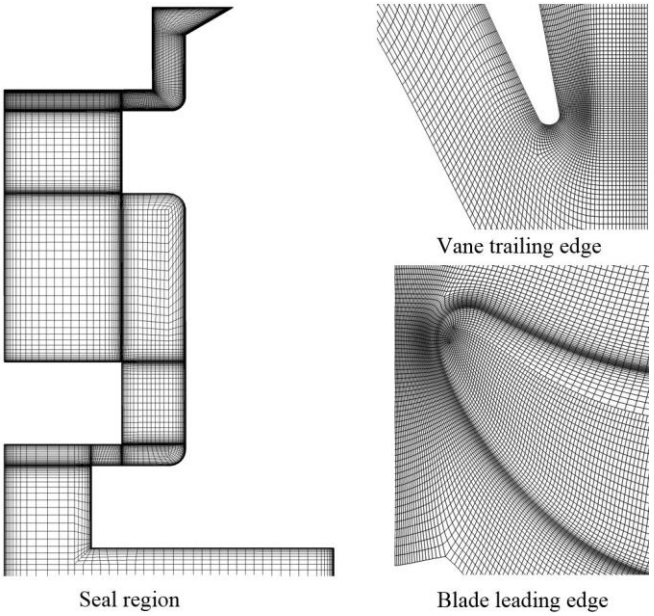

Figure 4: Mesh detail

4 TIME-AVERAGED FLOW CHARACTERISTICS

This section presents computed and measured distributions of pressure, swirl and effectiveness through the annulus and rim seal (section 4.1) and wheel-space (section 4.2).

4.1 Annulus and Rim Seal

The circumferential variation in time-averaged pressure on the hub, immediately upstream of the seal is shown in Figure 5. The non-dimensional pressure ($C_{p,a}$) is defined in the nomenclature. The silhouette indicates the measurement position, with flow from left to right. The two computational vane pitches represent the distribution across the full 22.5º sector modelled, while the experimental results represent two

instrumented vane pitches in the rig separated by 180º. The agreement between experimental and computational data is very good and provides validation that the pressure field in the annulus is captured well in the CFD. This is important as Owen [29] demonstrated a direct relationship between the peak-to-trough pressure difference and the level of ingress. The data presented is taken at Φ_0 = 0.03, although similarly good agreement was found at the other sealing flow rates computed. Note that Patinios et al. [26] have demonstrated that $C_{p,a}$ is virtually independent of Re_ϕ for a constant flow coefficient.

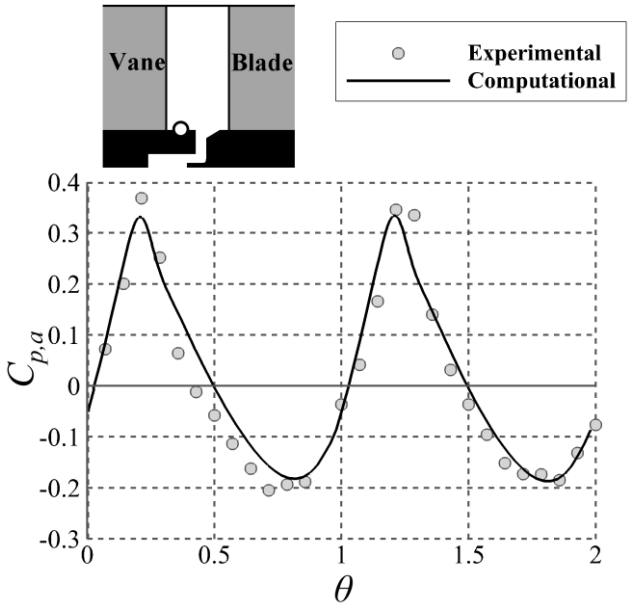

Figure 5: Circumferential distribution of pressure coefficient in annulus over two non-dimensional vane pitches (Φ_0 = 0.029, $Re_\phi = 1.0\times10^6$)

Effectiveness is based on the local concentration of CO_2 (c) relative to the concentration of CO_2 in the sealing (purge) flow (c_0) and annulus (c_a):

$$\varepsilon_c = \frac{c - c_a}{c_0 - c_a} \qquad (4.1)$$

Clearly, ε_c= 0 in the annulus and ε_c = 1 at all locations in a fully-purged wheel-space with no ingestion.

Figure 6 shows the computed contours of effectiveness and streamlines at a sealing flow rate where the wheel-space is fully purged. Egress from the wheel-space is entrained into the passage vortex with a strong influence near the suction surface of the blade. The egress is seen to clearly provide a tangible cooling effect to the rotor hub; as it migrates through the blade passage it mixes with the annulus flow with a gradual reduction in effectiveness. The interaction of the egress and passage vortex would likely introduce aerodynamic losses, though this is not the focus of this investigation.

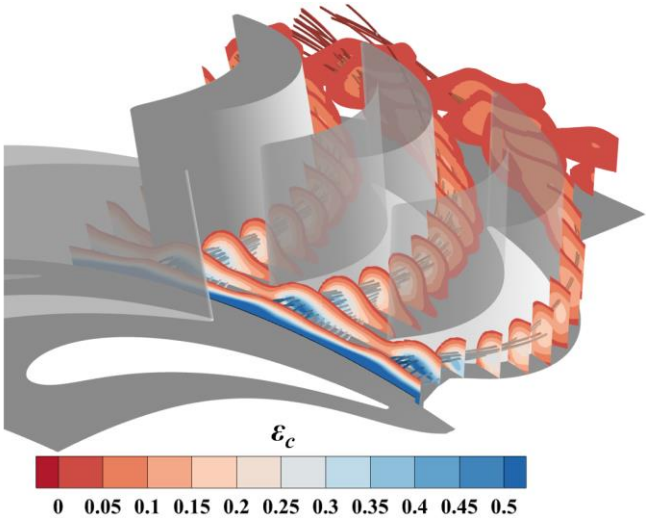

Figure 6: Contours of concentration-based effectiveness through the annulus (clipped to > 3%), with stream-traces originating from the seal (Φ_0 = 0.104, Re_ϕ = 1.0×10^6)

The radial movement of the egress and its entrainment into the passage vortex is illustrated in Figure 7. On the left of the figure, a computed isosurface of 5% effectiveness depicts migration of the egress as it traverses the rotor passage. This time-averaged data is shown in the rotating frame of reference. On the right of the figure the computation is compared with experimental data from the concentration probe, shown as radial traverses of effectiveness both upstream and downstream of the blade. The vertical axis is the non-dimensional radius (geometrically aligned with the left-hand

image of the turbine passage) which extends from r/b = 1 under the blade platform to $1.03 \leq r/b \leq 1.16$ across the annulus of height h = 25 mm. Scobie et al. [27] demonstrated that data collected with the two different-sized probes (outer diameters 1.0 and 1.7 mm) collapse to a single curve; further, experimental data collected at the two operating points show the concentration profiles are invariant with Re_ϕ.

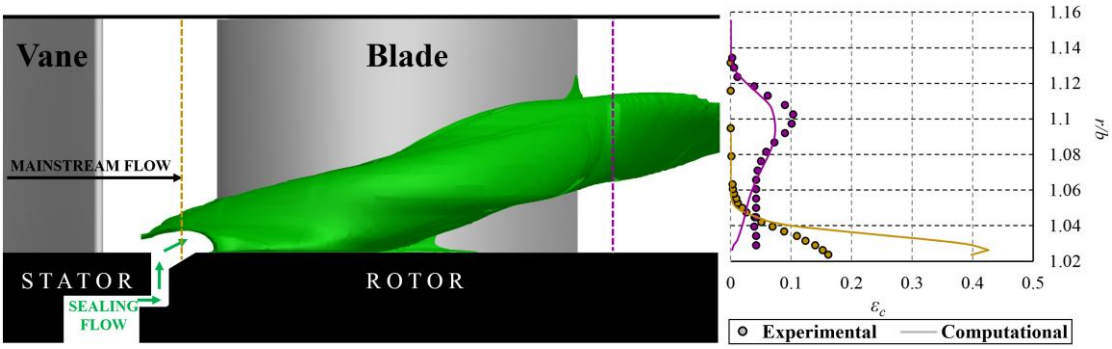

Figure 7: Concentration based sealing effectiveness through the annulus for Φ_0 = 0.104, $\mathrm{Re}_\phi = 1.0\times10^6$: isosurface of 5% effectiveness (left), radial traverses of effectiveness upstream and downstream of the blade (right)

For direct comparison, computational data was extracted at the same locations relative to the vane over one disc revolution, and then time-averaged. The downstream radial traverse shows good qualitative agreement and captures the radial movement of egress. The computational traverse upstream also captures ε_c well for $r/b > 1.04$, however there is a significant over-prediction for $r/b < 1.04$.

Figure 8 shows computed and measured concentration effectiveness (ε_c) for a radial traverse from the annulus into the centre-line of the seal clearance. Three sealing flow rates were used: Φ_0 = 0.021, 0.029 and 0.050. The data on the left is aligned with the right-hand-side silhouette of the seal and contours of computed distribution of effectiveness for Φ_0 = 0.021. The data shows ε_c = 0 in the annulus with an increase in

effectiveness through the rim seal-clearance as the ingress mixes with the egress pumped up the rotor.

The computations over-predict the measured levels of effectiveness in the rim seal and are unable to simulate the penetration of gas from the annulus into the rotating flow. It is speculated this is a consequence of the inadequacy of a RANS turbulence model. More realistic modelling may be found with LES, as discussed by Chilla *et al*. [14].

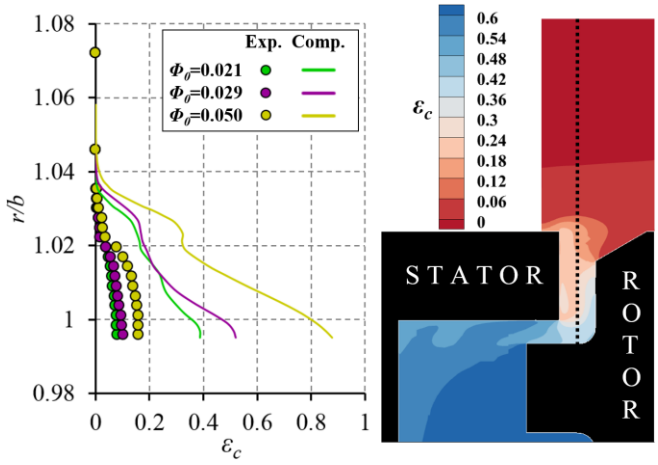

Figure 8: Concentration based sealing effectiveness through the seal at $Re_\phi = 1.0\times10^6$: radial traverse measurements into the seal (left), contours of computational distribution at $\Phi_0 = 0.021$ (right)

4.2 Wheel-space

In this section numerical simulations of concentration-effectiveness (ε_c) and swirl in the wheel-space are compared with experiments.

Both experimentally and computationally, the inner wheel-space is fully sealed ($\varepsilon_c = 1$) for $\Phi_0 > 0.02$. A decision to restrict computations to a range above this value was based on previous work; experience identified the slow convection of ingested fluid through the inner wheel-space led to prohibitively-large computational effort required to reach convergence.

Figure 9 (a/b) show the radial variation of ε_c for Φ_0 = 0.021 and 0.029 respectively. Discrete measurements were taken on the stator disc (circle symbols) and in the rotating-core (triangle symbols), and continuous levels of computed values are shown as solid and dotted lines respectively. A silhouette of the overlap seal is included alongside the figure with superposed contours of computed ε_c; the silhouette is aligned with the radial position in the ordinate. There is good qualitative agreement between shapes of experimental and computational curves, but with an overall under-prediction of ingress.

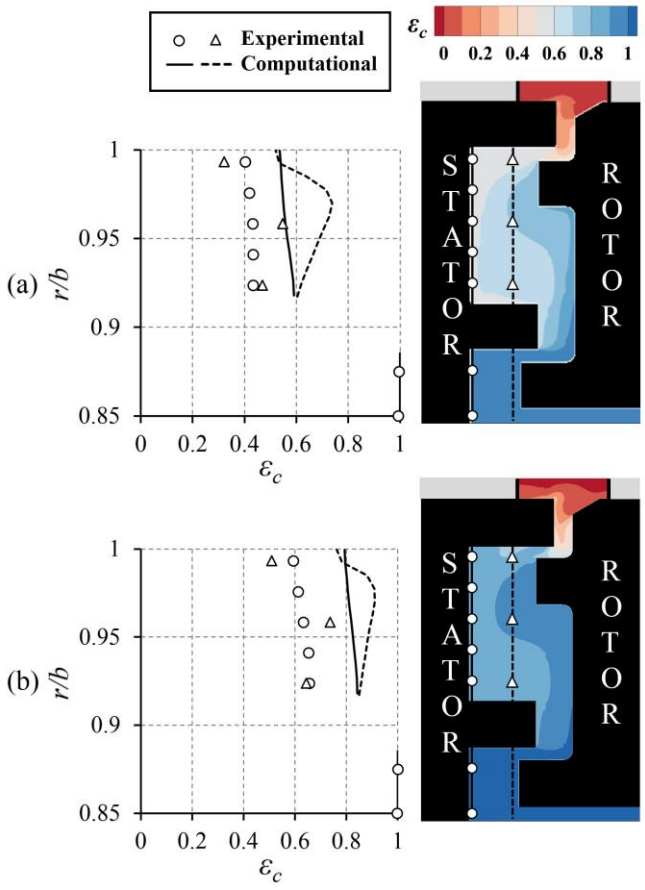

Figure 9: Concentration based sealing effectiveness in the wheel-space at $Re_\phi = 1.0\times10^6$: (a) Φ_0 = 0.021, (b) Φ_0 = 0.029

The figures illustrate an abrupt increase in sealing effectiveness from ε_c = 0 in the annulus across the outer seal. There is a further increase in effectiveness across the inner

seal, with no penetration of ingress to a fully-sealed inner wheel-space where $\varepsilon_c = 1$. The experiments show the concentration on the stator disc is invariant with radius for $r/b < 0.96$, with essentially-complete mixing between ingress and egress as the ingested fluid enters the wheel-space as the source for the stator boundary layer. The computations do not quite simulate this uniform commixture. The effectiveness in the core is influenced by high-concentration fluid from the rotor boundary layer which is pumped radially outwards. The flow structure differs from the classical Batchelor flow with an inviscid core of fluid moving axially from the stator to rotor boundary layers.

Similar observations can be made in both Figure 9 a and b. As expected, ε_c increases with increasing Φ_0 (hence λ_T) and the purge flow pressurises the wheel-space relative to the annulus.

Figure 10 shows the variation of effectiveness with Φ_0 in both the inner ($r/b < 0.85$) and outer wheel-spaces, with concentration measurements made on the stator disc at r/b = 0.958 and 0.85 respectively. In all cases ε_c increases with increasing Φ_0, as the sealing flow pressurises the wheel-space and reduces ingress through the rim-seal. The experimental data were collected at the two operating points (Table 1) at different rotational Reynolds numbers, and collapse onto individual curves. The four computed cases are shown as red symbols for the higher Re_ϕ.

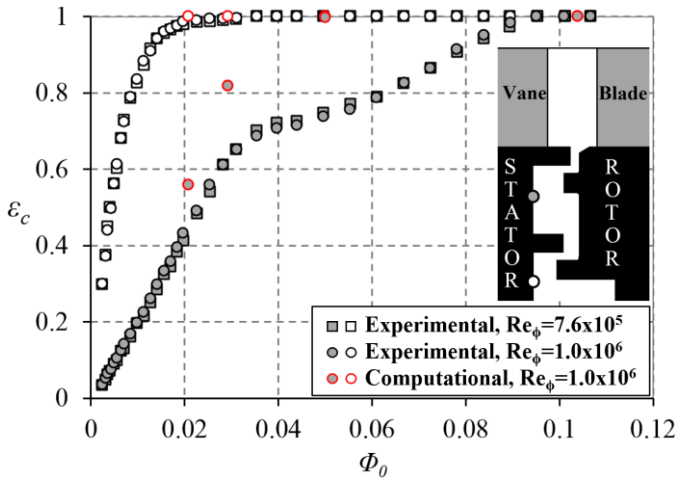

Figure 10: Variation in wheel-space concentration effectiveness with non-dimensional sealing parameter

As discussed above there is an under-prediction of ingress in the outer wheel-space and the CFD has not captured the inflexion or *kink* in the experimental data between $0.05 < \Phi_0 < 0.07$. The ε_c - Φ_0 curve does not follow the form predicted by theoretical models [29] and section 5 discusses how strong unsteady pressure fluctuations are measured (though not computed) within this range of purge flow rates. Similar shaped curves have been published by Boudet *et al*. [8], Gentilhomme *et al*. [30] and Clark *et al*. [31], but the authors do not discuss what drives the phenomenon.

Profiles of swirl (β) in the wheel-space and into the annulus are shown in Figure11 for four sealing flow rates. As expected, increasing the turbulent flow parameter reduces the corresponding swirl level. There is good general agreement between experiment and computation, with the exception of r/b = 0.993. However, at this outer wheel-space location there may be sensitivity to probe measurements in proximity to the boundary layers. The figure also indicates the high levels of shear found in the outermost region of the seal that potentially give rise to Kelvin-Helmholtz instabilities, as discussed in Section 5.

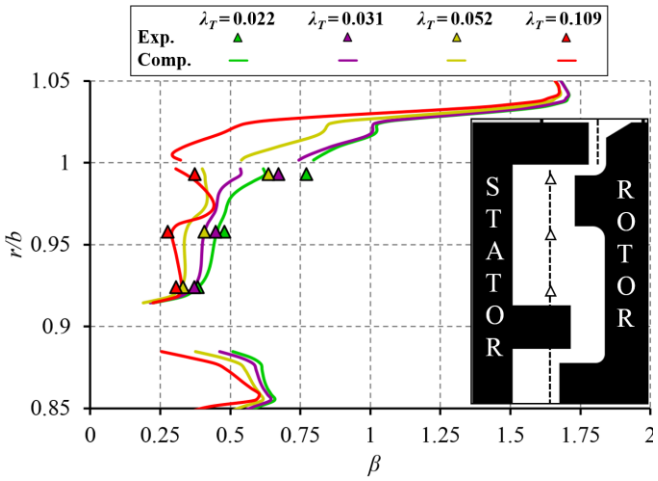

Figure 11: Variation in swirl at $Re_\phi = 1.0\times10^6$

5 UNSTEADY FLOW CHARACTERISTICS

As discussed in the literature review and illustrated in Figure 1, numerous computational and experimental studies have identified unsteady flow structures with the potential to influence ingress. Both the cause and effect of the phenomenon is not well understood.

Fast Fourier Transforms of the pressure at $r/b = 0.993$ on the stator disc are presented in Figure 12 for four purge flow rates. The top silhouette indicates the monitoring point and the pressure amplitudes have been normalised, as detailed in the nomenclature. The frequencies were normalised by the rotational disc frequency, f_d. The analysis was performed over the final computed revolution of the disc and required transformation of data from the rotating to stationary frame at 240 equally-spaced timesteps. This transformation was performed in two parts: for each timestep the sector was rotated to its time-resolved physical position and duplicated over 360 degrees (using the TRACE post-processing tool POST), this modified data set was then imported into Tecplot 360 EX 2015 where time-resolved data was extracted at locations defined in the stationary frame of reference.

In Figure 12, $f / f_d = 48$ corresponds to the blade passing frequency (BPF). Intensity at this frequency is seen across all sealing flow rates, strengthening at higher purge. At the two lowest purge conditions (a/b), low frequencies (*i.e.* $f / f_d \sim 13$ to 14) dominate the spectrum; their intensity diminish with increasing sealing flow, suggesting rotating structures are associated with ingress at low purge. Analysis shows these energy peaks correspond to $N = 16$ low-pressure structures rotating at 0.85 of the disc speed, which is consistent with data from the literature presented in Figure 1. Details of the computed and measured variation of N, ω/Ω and Φ_0 for this study are summarised in Table 2.

As the sealing flow rate increased to $\Phi_0 = 0.050$ (c), the low-frequency energy significantly reduces in magnitude and the frequency increases slightly to $f / f_d \sim 15$, corresponding to the $N = 16$ low-pressure structures rotating at $\omega/\Omega = 0.94$. A second harmonic of this frequency also strengthens due to strength of the BPF at this purge. Note that the additional peak frequencies (at $f / f_d = 34$, 35 and 33 in Figures 12abc respectively) result from non-linear combinations of low frequencies and the BPF: (a) 34 = 48-14, (b) 35 = 48-13, and (c) 33 = 48-15. A similar interaction between frequencies was observed by Boudet *et al*. [8] in FFTs of their computations. At the highest purge ($\Phi_0 = 0.104$) no clear frequency peaks exist below the normalised BPF, although there is a broad spectrum of activity at reduced magnitude.

To investigate the influence of the 22.5º sector, an enlarged 67.5º sector was used to compute the intermediate purge case with $\Phi_0 = 0.029$. The simulation was initialised from the converged 22.5º model, which was duplicated to form the larger sector. The larger model was then run for a further five revolutions, allowing changes in the unsteady flow structure to form. There was no significant change to the computed level of ingress and the FFT analysis for the two sectors (shown in Figure 12 (b)) was largely similar. Furthermore, $N = 16$ was dominant for both sector sizes. This is the greatest

common divisor of both blade and vane count, therefore indicating that vanes and blades may not only supress the unsteady structures [13, 20], but may also influence their count. The speed, size and number of unsteady flow structures determined from a full 360º model is unknown; however the quantitative similarities between the 22.5º and 67.5º sectors provides confidence that sector models can be used in numerical simulations of ingress.

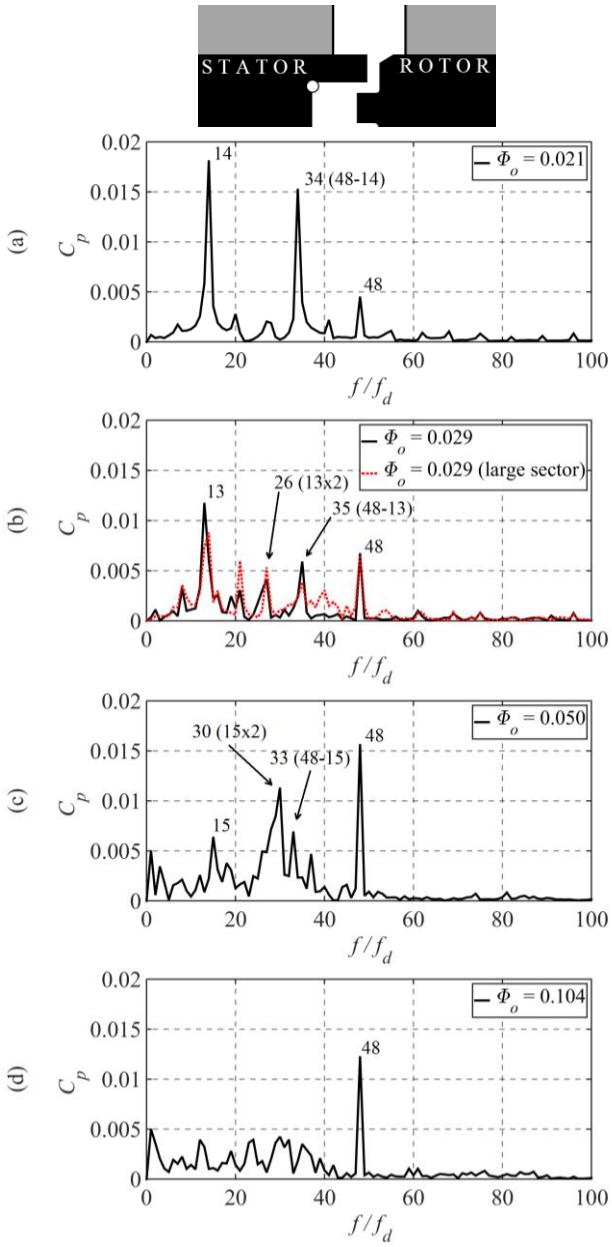

Figure 12: Fast Fourier Transforms of unsteady computational data at r/b = 0.993 and $Re_\phi = 1.0\times10^6$

Fast Fourier Transforms of unsteady pressure at various radial locations through the seal are shown in Figure13. The top silhouette indicates the four colour-coded monitoring points. All data presented is for $\Phi_0 = 0.021$, as the strongest unsteadiness occurs at low purge. The same frequencies identified at $r/b = 0.993$ on the stator disc exist at higher radii through the seal, with additional high frequencies in locations closer to the annulus. Note that Figure 12 (a) and Figure 13 (a) present the same data but the different scale in Figure 13 allows the greater unsteadiness found within the seal to be clearly shown. As discussed above, additional frequencies are attributed to non-linear combinations of the fundamental low frequency and the BPF. Unsurprisingly the strength of the normalised blade passing frequency magnifies at monitoring points closer to the blade row. Interestingly, the dominant low frequency ($f / f_d = 14$) is strongest in the axial clearance, where the annulus flow first interacts with the wheel-space flow. This is consistent with the origin of the large-scale structures being Kelvin-Helmholtz instabilities [13] created by the shear between two flows; here the highly-swirled flow immediately downstream of the vane meets the relatively low-swirling egress in the outer part of the seal.

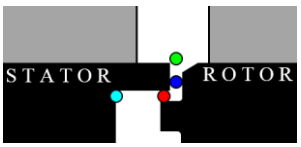

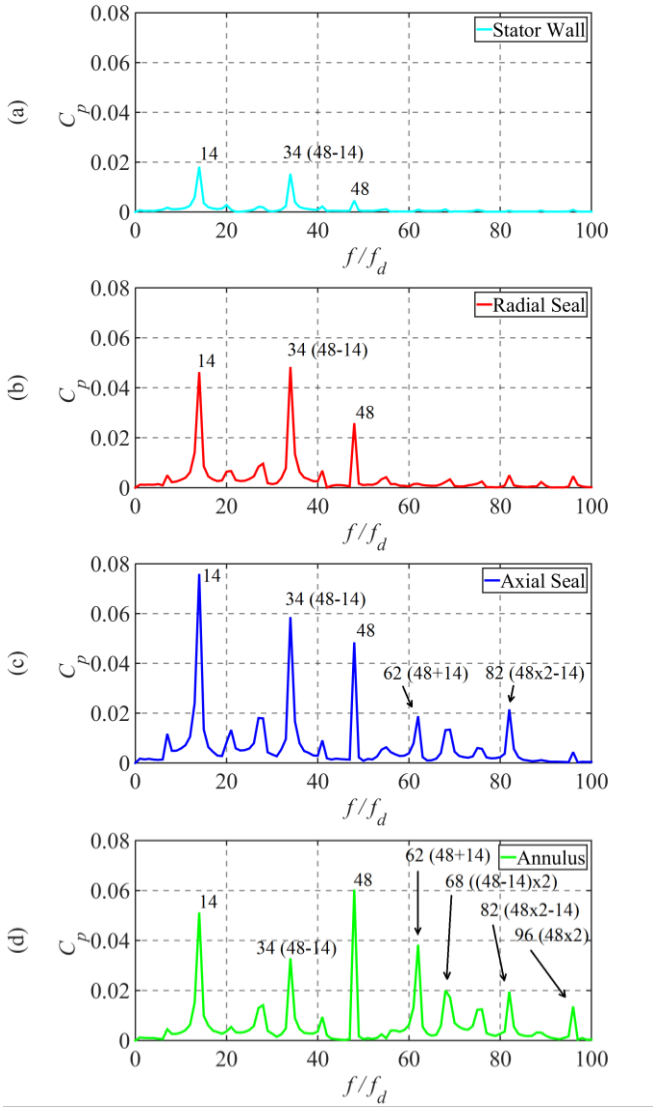

Figure 13: Fast Fourier Transforms of unsteady computational data at four locations through the seal: Φ_0 = 0.021; $Re_\phi = 1.0\times10^6$

The formation of Kelvin-Helmholtz instabilities in a shear layer is depicted schematically in Figure 14. If the two layers are assumed inviscid and separated by an infinitely thin vortex sheet of uniform vorticity, any small perturbation will cause a slight billowing of the vortex sheet as shown by Figure 14 (a/b). However, this billowing results in localised regions of higher and lower pressure as the local velocities decrease and increase respectively. This fundamentally unstable state, where the local changes in pressure act to increase the size of the billowing, is shown in Figure 14 (c).

The two layers quickly wrap into a large vortex. This phenomenon can occur at different length scales, with smaller vortices encompassed by larger ones, as shown by Figure 14 (e).

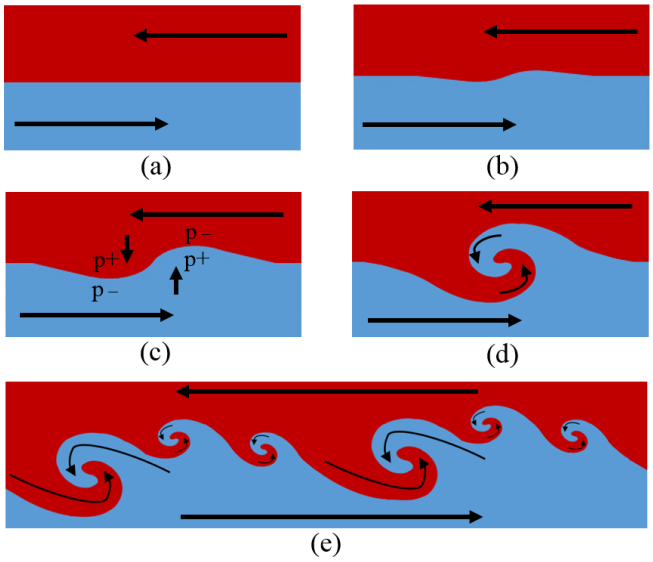

Figure 14: The formation of Kelvin Helmholtz instabilities

Vortical flow structures similar to Kelvin-Helmholtz instabilities have been captured in the numerical simulations, as shown in Figure 15. This figure shows contours of effectiveness and streamlines on different planes *through* the seal, as indicated by the dotted line in the silhouette. The instantaneous flow fields are taken in the rotating frame and therefore the wheel-space and annulus flows appear to counter rotate. The computational sector has been duplicated for post-processing and two purge flow rates were used.

Six individual structures form at both sealing flow rates, corresponding to low pressure regions aligned with the blade passages; these are relatively stable and rotate at the disc speed. However, at the low sealing flow rate (Figure 15 (a)) these smaller structures appear to coalesce into larger structures, typical of Kelvin-Helmholtz instabilities. It is this larger unstable structure that rotates at just less than the disc speed

and drives ingress deeper into the wheel-space. For $\Phi_0 = 0.021$, $N = 16$ and $\omega/\Omega = 0.85$, Figure 15 (b) shows that these larger structures are completely suppressed at the higher purge and the six smaller vortical structures are reduced in size. Savov and Atkins [21] discuss a gap recirculation zone (GRZ) in the seal clearance, the size of which is influenced by the purge flow rate. At high purge the GRZ is blown out and it is speculated this phenomenon influences the structures shown here.

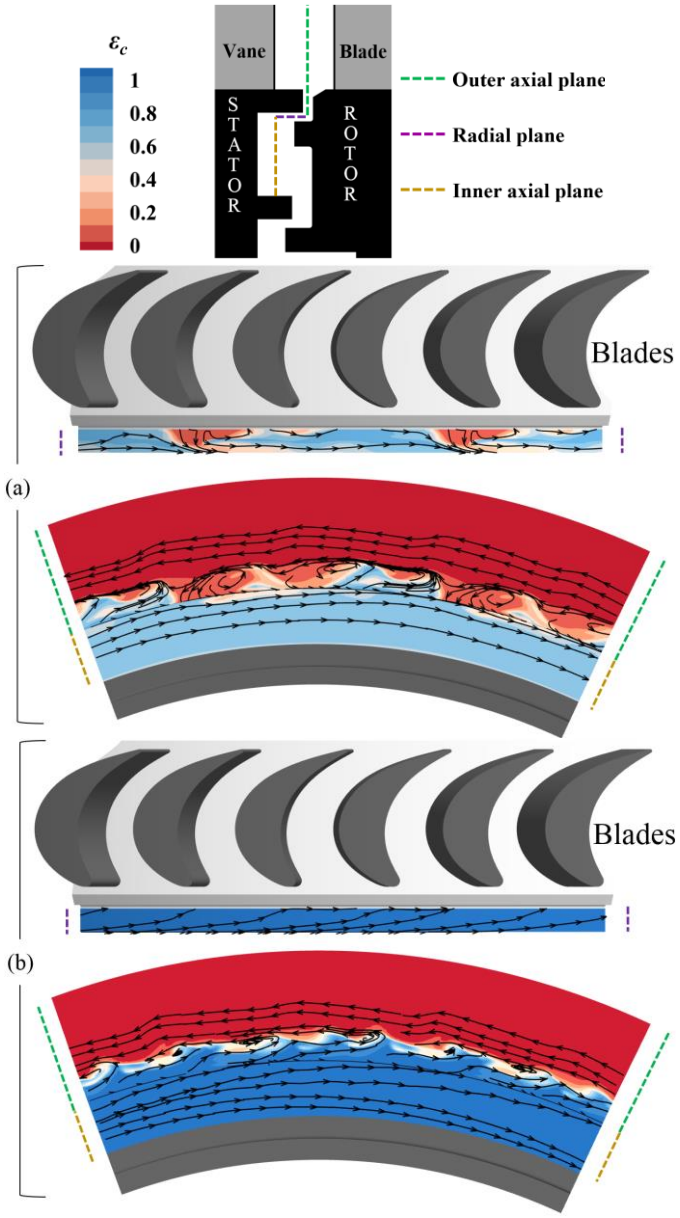

Figure 15: Instantaneous contours of effectiveness through the rim seal with streamlines taken in the rotational frame and with the stator hidden: (a) Φ_0 = 0.021, (b) Φ_0 = 0.104

Experimental measurements of the unsteady pressure field at r/b = 0.993 on the stator disc are shown in Figure 16, in the form of an FFT analysis similar to that used for the computations presented in Figure 12. Data is shown for five purge flow rates and the two rotational Reynolds numbers (Table 1). The normalised frequencies at which the spectral activity occurs are largely invariant with Re_ϕ. The experiments were conducted with and without the pitot tubes shown in Figure 2, to confirm they had no measurable effect on the unsteady phenomena. The experiments exhibit unsteady pressure fluctuations at frequencies significantly below the BPF, similar to those modelled computationally. For the experiments f / f_d ~ 25 *vs.* f / f_d ~ 14 for the computations. As with the computations, the amplitude of the low-frequency energy reduces with increasing purge (apart from the case Φ_0 = 0.050 as discussed below) and is largely supressed at Φ_0 = 0.104.

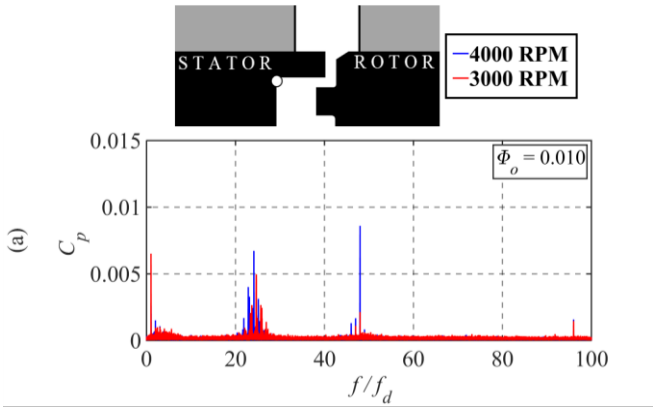

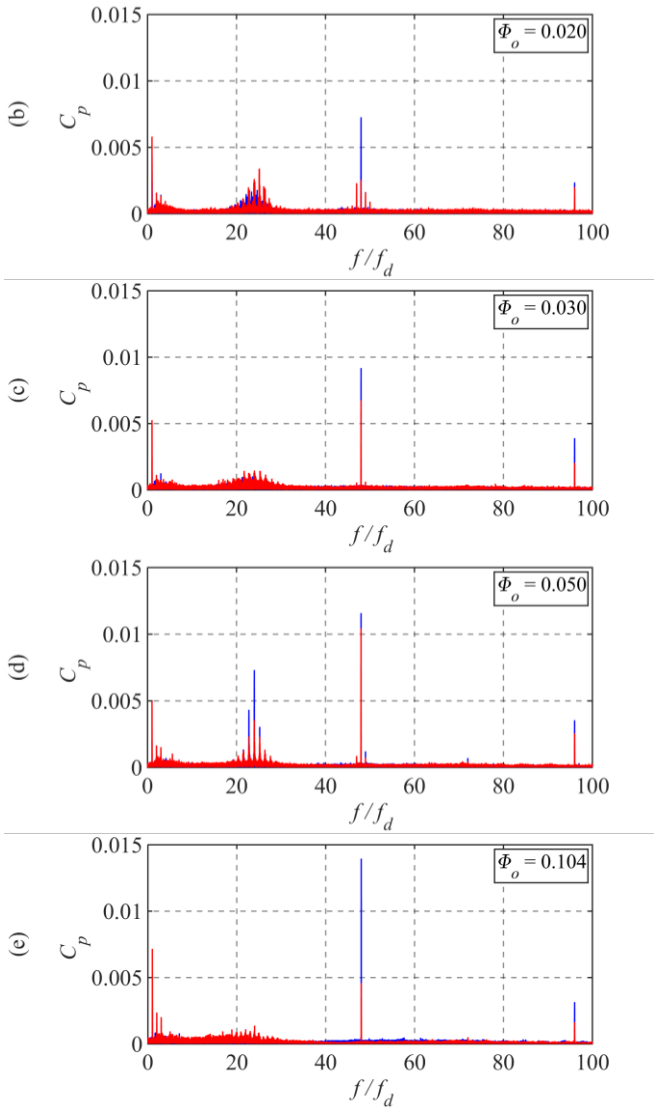

Figure 16: Fast Fourier Transforms of unsteady experimental data at *r*/*b* = 0.993 on the wheel-space stator wall

The rotational speed (ω/Ω) and number (N) of the structures was determined from two transducers circumferentially displaced by an angle α = 8°, using the method of analysis used by Beard *et al*. [23]. Data was recorded at 100 kHz for 10 s, with the signals divided into single revolutions of the disc and filtered to remove frequencies outside the region of interest. The signals from each pressure transducer were cross-correlated for each disc revolution. A histogram recording the lag-time from the peak in each cross-correlation was then populated to determine the lag time (Δt_α) between the transducers, leading to the rotational speed of the structures ($\omega = \alpha/\Delta t_\alpha$). The number

of structures around the circumference (N) follows from the normalised frequency (f / f_d) and rotational speed (ω/Ω). The data is presented in Table 2 with the corresponding computational values. It should be noted that no rotating structures are identified at $\Phi_0 = 0.104$.

At the three lowest sealing flow rates the spectral activity at $f / f_d \sim 25$ (*i.e.* ~ 0.52 of the BPF) corresponds to 25/26 structures rotating at 0.92-0.96 of the disc speed. These can be compared to the 16 structures determined from the computations. Curiously there is a magnification of the low-frequency activity at $\Phi_0 = 0.050$, as shown in Figure 16 (d). This behaviour is distinct from that measured over the range $\Phi_0 = 0.01$-0.03, as $f / f_d = 24$ precisely (*i.e.* half the blade count) and the corresponding structures are calculated, within experimental uncertainty, to rotate at the disc speed ($\omega/\Omega = 1$). The existence of these structures is believed to be linked to the inflection in the effectiveness curve shown in Figure 10, given the occurrence of both at $\Phi_0 = 0.050$. Although this connection cannot yet be proved, the amplitude of the unsteady pressure corresponding to these structures is sudden and significant, and would be expected to have an influence on the effectiveness level in Figure 10. Additionally, in other experiments with the blades removed from the rig, both the inflection in Figure 10 and the large magnification in activity at $\Phi_0 = 0.050$ were not seen. Neither phenomena were seen in computations.

Case	Rotor Speed (RPM)	Non-dimensional Sealing Parameter (Φ_0)	Number of Structures (N)	Rotational speed of Structures (ω/Ω)
Comp.	4000	0.021	16	0.88
Comp.	4000	0.029	16	0.81
Comp.	4000	0.050	16/32	0.94
Comp	4000	0.104	N.A.	N.A
Exp.	4000	0.010	26	0.93
Exp.	4000	0.020	26	0.93
Exp.	4000	0.030	25	0.93
Exp.	4000	0.050	24	0.99
Exp.	4000	0.104	N.A.	N.A
Exp.	3000	0.010	26	0.94
Exp.	3000	0.020	26	0.96
Exp.	3000	0.030	26	0.92
Exp.	3000	0.050	23	1.03
Exp.	3000	0.104	N.A.	N.A.

Table 2: Comparison of large scale flow structures: experiment and computation

The fundamental unsteady behaviour measured in the rig appears to have been captured by the computations, although differences between the computational and experimental results include the following: different numbers of unsteady structures around the disk (N = 16/32 in computations, N = 24-26 in experiments); frequencies measured at 1-3 times the disc-passing frequency that are attributed to imperfections in the disc; and a second measured harmonic of the BPF. The additional peaks in the computational frequency spectrum created from non-linear combinations of low frequencies and the BPF are not seen experimentally. The significantly higher resolution of the experimental FFTs is a result of data being recorded over 500 revolutions, where the computational data could only be sampled over a single revolution.

6 CONCLUSIONS

- URANS computations using a sector model have been compared to experimental data from an axial turbine rig, providing insight into the fluid dynamics of ingress.

- An accurate numerical simulation of the annulus pressure distribution is demonstrated, which shows egress entrained into the passage vortex.
- The qualitative features of the flow structure in the seal-clearance and wheel-space were captured, but it is speculated that a quantitative under-prediction of ingress is due to inadequacies in the turbulence modelling.
- Unsteady computational analysis determined N = 16 low-pressure structures rotating at ≈ 0.85 of the disc speed; these are identified as fundamental to ingress. It is hypothesised that the physical origin of such phenomenon is Kelvin-Helmholtz instabilities caused by the tangential shear between the annulus and egress flows. Their existence and influence is highly sensitive to sealing flow rate and they were fully supressed at the high purge.
- The experimental data supported the existence of the large-scale structures and showed they are largely invariant to Rotational Reynolds number. The data shows $23 < N < 26$ rotating at ≈ 0.95 of the disc speed, and that the structures reduce in intensity with increasing purge.
- A magnification of the low-frequency activity at $\Phi_0 = 0.050$, corresponding to exactly 24 structures rotating at the disc speed, is believed to drive an inflection in the relationship between ε_c *and* Φ_0.
- Computations from an increased sector size resulted in minor changes to the strength of the large scale unsteadiness, but with no significant changes in the level of ingress.

ACKNOWLEDGMENT

The authors would like to thank Siemens and the Engineering and Physical Sciences Research Council for their financial support. Generous technical support was provided

by Kunyuan Zhou and Vincent Peltier at Siemens and Graham Ashcroft at the Institute of Propulsion Technology of DLR. This research made use of the Balena High Performance Computing Service at the University of Bath.

Data Access: Due to confidentiality agreements with research collaborators, supporting data can only be made available to bona fide researchers subject to a nondisclosure agreement. Details of how to request access are available at the University of Bath data archive: http://dx.doi.org/10.15125/BATH-00116.

NOMENCLATURE

A_p	amplitude of unsteady pressure
b	radius of seal (m)
BPF	blade passing frequency (Hz)
c	concentration of tracer gas
CFD	computational fluid dynamics
CFL	Courant–Friedrichs–Lewy
C_F	flow coefficient ($=W/(\Omega b)$)
C_p	pressure coefficient ($= A_p / (0.5\,\rho\Omega^2 b^2)$)
$C_{p,a}$	pressure coefficient in annulus ($= (p_a - \bar{p}_a)/(0.5\,\rho\Omega^2 b^2)$)
$C_{w,0}$	non-dimensional sealing flow rate ($= \dot{m}/(\mu b)$)
DLR	Deutsches Zentrum für Luft- und Raumfahrt
f	measured frequency (Hz)
f_d	frequency of disk rotations (Hz)
FFT	fast Fourier transform
G_c	seal-clearance ratio ($= s_{c,ax}/b$)
LES	large eddy simulation

$\dot{m}$ mass flow rate (kg/s)

M Mach number

N Number of large-scale structures around disc

p static pressure (Pa)

r radius (m)

Re_w axial Reynolds number in annulus based on radius (= $\rho W b/\mu$)

Re_ϕ rotational Reynolds number (= $\rho \Omega b^2/\mu$)

RPM revolutions per minute

SST shear stress transport

s_c seal clearance (m)

TET turbine entry temperature

TRACE Turbomachinery Research Aerodynamics Computational Environment

U bulk mean radial seal velocity (= $\dot{m}_0/(2\pi\rho b s_c)$)

URANS unsteady Reynolds-averaged Navier-Stokes simulation

V_ϕ tangential velocity (m/s)

W axial velocity in annulus (m/s)

z axial coordinate (m)

α angle between unsteady pressure transducers (rad)

β swirl ratio (= $V_\phi/(\Omega r)$)

Δt_α time for large scale structure to move through angle α (s)

ε effectiveness

ε_c concentration effectiveness

λ_T turbulent flow parameter (= $C_{w,0}\mathrm{Re}_\phi^{-0.8}$)

μ dynamic viscosity (kg/(ms))

ρ density (kg/m^3)

Φ_0 non-dimensional sealing parameter (= $U/(\Omega b)$)

ω angular speed of large scale structures (rad/s)

Ω angular speed of rotating disk (rad/s)

Subscripts

a annulus

0 sealing flow

References

[1] Diakunchak, I., Kiesow, H.J. & McQuiggan, G., 2008, "The history of the Siemens gas turbine," ASME Paper GT2008-50507.

[2] Scobie, J. A., Sangan, C. M., Owen, J. M., and Lock, G. D., 2016, "Review of Ingress in Gas Turbines," ASME J. Eng. Gas Turb. Power, 138(12), p. 120801.

[3] Bohn, D., Rudzlnskl, B., Surken, N. & Gartner, W., 2000, "Experimental and numerical investigation of the influence of rotor blades on hot gas ingestion into the upstream cavity of an axial turbine stage," ASME Paper 2000-GT-284.

[4] Hills, N.J., Chew, J.W. & Turner, A.B., 2002, "Computational and mathematical modeling of turbine rim seal ingestion," ASME J. Turbomach., 124(2), pp. 306-315.

[5] Laskowski, G.M., Bunker, R.S., Bailey, J.C., Ledezma, G., Kapetanovic, S., Itzel, G.M., Sullivan, M.A. & Farrell, T.R., 2011, "An Investigation of Turbine Wheelspace Cooling Flow Interactions With a Transonic Hot Gas Path—Part II: CFD Simulations," ASME J. Turbomach., 133(4), p. 041020.

[6] Cao, C., Chew, J.W., Millington, P.R. & Hogg, S.I., 2004, "Interaction of rim seal and annulus flows in an axial flow turbine," ASME J. Eng. Gas Turb. Power, 126(4), pp. 786-793.

[7] Jakoby, R., Zierer, T., Lindblad, K., Larsson, J., deVito, L., Bohn, D. E., Funcke, J., and Decker, A., 2004, "Numerical Simulation of the Unsteady Flow Field in an Axial Gas Turbine Rim Seal Configuration," ASME Paper No. GT2004-53829.

[8] Boudet, J., Autef, V., Chew, J., Hills, N. & Gentilhomme, O., 2005, "Numerical simulation of rim seal flows in axial turbines," Aeronautical Journal, 109(1098), pp. 373-383.

[9] Boudet, J., Hills, N.J. & Chew, J.W., 2006, "Numerical Simulation of the Flow Interaction between Turbine Main Annulus and Disc Cavities," ASME Paper No. GT2006-90307.

[10] Julien, S., Lefrancois, J., Dumas, G., Boutet-Blais, G., Lapointe, S., Caron, J.-F. & Marini, R., 2010, "Simulations of flow ingestion and related structures in a turbine disk cavity," ASME Paper No. GT2010-22729.

[11] Boutet-Blais, G., Lefrancois, J., Dumas, G., Julien, S., Harvey, J.-F., Marini, R. & Caron, J.-F., 2011, "Passive Tracer Validity for Cooling Effectiveness Through Flow Computation in a Turbine Rim Seal Environment," ASME Paper No. GT2011-45654.

[12] Feiereisen, J., Paolillo, R. & Wagner, J., 2000, "UTRC Turbine Rim Seal Ingestion and Platform Cooling Experiments," AIAA Paper No. AIAA-2000-3371.

[13] Rabs, M., Benra, F.K., Dohmen, H.J. & Schneider, O., 2009, "Investigation of flow instabilities near the rim cavity of a 1.5 stage gas turbine," ASME Paper No. GT2009-59965.

[14] Chilla, M., Hodson, H. & Newman, D., 2013, “Unsteady interaction between annulus and turbine rim seal flows,” ASME J. Turbomach., 135(5), p. 051024.

[15] O'Mahoney, T.S.D., Hills, N.J., Chew, J.W. & Scanlon, T., 2011, “Large-Eddy simulation of rim seal ingestion,” Journal of Mechanical Engineering Science, 225(12), pp. 2881-2891.

[16] O'Mahoney, T., Hills, N. & Chew, J., 2012, “Sensitivity of LES results from turbine rim seals to changes in grid resolution and sector size,” Progress in Aerospace Sciences, 52, pp. 48-55.

[17] Wang, C.-Z., Mathiyalagan, S., Johnson, B.V., Glahn, J.A. & Cloud, D.F., 2014, “Rim seal ingestion in a turbine stage from 360 degree time-dependent numerical simulations”. ASME J. Turbomach., 136(3), p. 031007.

[18] Mirzamoghadam, A.V., Kanjiyani, S., Riahi, A., Vishnumolakala, R. & Gundeti, L., 2014, “Unsteady 360 Computational Fluid Dynamics Validation of a Turbine Stage Mainstream/Disk Cavity Interaction”. ASME J. Turbomach, 137(1), p. 011008.

[19] Town, J., Averbach, M. & Camci, C., 2016, “Experimental and Numerical Investigation of Unsteady Structures Within the Rim Seal Cavity in the Presence of Purge Mass Flow,” ASME Paper No. GT2016-56500.

[20] Savov, S.S., Atkins, N.R. & Uchida, S., 2017, “A Comparison of Single and Double Lip Rim Seal Geometries,” ASME J. Eng. Gas Turb. Power, 139(11), p. 112601.

[21] Savov, S.S. & Atkins, N.R., 2017, “A Rim Seal Ingress Model Based on Turbulent Transport,” ASME Paper No. GT2017- 63531.

[22] Zlatinov, M.B., Tan, C.S., Little, D. & Montgomery, M., 2016, “Effect of Purge Flow Swirl on Hot-Gas Ingestion into Turbine Rim Cavities,” Journal of Propulsion and Power, 32(5), pp. 1055-1066.

[23] Beard, P.F., Gao, F., Chana, K.S. & Chew, J., 2017, “Unsteady Flow Phenomena in Turbine Rim Seals,” ASME J. Eng. Gas Turb. Power, 139(3), p. 032501.

[24] Gao, F., Chew, J., Beard, P.F., Amirante, D. & Hills, N.J., 2017, “Numerical Studies of Turbine Rim Sealing Flows on a Chute Seal Configuration,” Proceedings of 12th European Conference on Turbomachinery Fluid dynamics & Thermodynamics, p. ETC2017-284.

[25] Schadler, R., Kalfas, A.I., Abhari, R.S., Schmid, G. & Voelker, S., 2017, “Modulation and radial migration of turbine hub cavity modes by the rim seal purge flow,” ASME J. Turbomach., 139(1), p. 011011.

[26] Patinios, M., Scobie, J.A., Sangan, C.M., Michael Owen, J. & Lock, G.D., 2016, “Measurements and Modeling of Ingress in a New 1.5-Stage Turbine Research Facility,” ASME J. Eng. Gas Turb. Power, 139(1), p. 012603.

[27] Scobie, J.A., Hualca, F.P., Patinios, M., Sangan, C.M., Owen, J.M. & Lock, G.D., 2017, “Re-Ingestion of Upstream Egress in a 1.5-Stage Gas Turbine Rig,” ASME Paper No. GT2017-64620.

[28] Owen, J. M., and Rogers, R. H., 1989, Flow and Heat Transfer in Rotating-Disc Systems, Volume 1—Rotor Stator Systems, Research Studies Press Ltd, UK.

[29] Owen, J. M., 2011, “Prediction of Ingestion through Turbine Rim Seals. Part II: Externally Induced and Combined Ingress,” ASME J. Turbomach., 133(3), p. 031006.

[30] Gentilhomme, O., Hills, N.J., Turner, A.B. & Chew, J.W., 2003, “Measurement and Analysis of Ingestion Through a Turbine Rim Seal,” ASME J. Turbomach., 125(3), pp. 505-512.

[31] Clark, K., Barringer, M., Johnson, D., Thole, K., Grover, E. & Robak, C., 2017, “Effects of Purge Flow Configuration on Sealing Effectiveness in a Rotor-Stator Cavity,” ASME Paper No. GT2017-63910.